

## Seismic interferometry applied to local fracture seismicity recorded at Planchón-Peteroa Volcanic Complex, Argentina-Chile

Casas, J. A.; Draganov, D.; Badi, G. A.; Manassero, M. C.; Olivera Craig, V. H.; Franco Marín, L.; Gómez, M.; Ruigrok, E.

**DOI**

[10.1016/j.jsames.2019.03.012](https://doi.org/10.1016/j.jsames.2019.03.012)

**Publication date**

2019

**Document Version**

Accepted author manuscript

**Published in**

Journal of South American Earth Sciences

**Citation (APA)**

Casas, J. A., Draganov, D., Badi, G. A., Manassero, M. C., Olivera Craig, V. H., Franco Marín, L., Gómez, M., & Ruigrok, E. (2019). Seismic interferometry applied to local fracture seismicity recorded at Planchón-Peteroa Volcanic Complex, Argentina-Chile. *Journal of South American Earth Sciences*, 92, 134-144. <https://doi.org/10.1016/j.jsames.2019.03.012>

**Important note**

To cite this publication, please use the final published version (if applicable).  
Please check the document version above.

**Copyright**

Other than for strictly personal use, it is not permitted to download, forward or distribute the text or part of it, without the consent of the author(s) and/or copyright holder(s), unless the work is under an open content license such as Creative Commons.

**Takedown policy**

Please contact us and provide details if you believe this document breaches copyrights.  
We will remove access to the work immediately and investigate your claim.

## Seismic interferometry applied to regional and teleseismic events recorded at Planchón-Peteroa Volcanic Complex, Argentina-Chile

Casas, José Augusto<sup>a</sup>, Draganov, Deyan<sup>b</sup>, Badi, Gabriela Alejandra<sup>c</sup>, Franco, Luis<sup>d</sup>

<sup>a</sup>*Facultad de Ciencias Astronómicas y Geofísicas, Universidad Nacional de La Plata, CONICET, Argentina*

<sup>b</sup>*Department of Geoscience and Engineering, Delft University of Technology, The Netherlands*

<sup>c</sup>*Facultad de Ciencias Astronómicas y Geofísicas, Universidad Nacional de La Plata, Argentina*

<sup>d</sup>*Observatorio Volcanológico de los Andes del Sur (OVDAS-SERNAGEOMIN), Chile*

---

### Abstract

The Planchón-Peteroa Volcanic Complex (PPVC) is located in the Central Andes, Argentina-Chile. Even though this active volcanic system is considered one of the most dangerous volcano in the region, with more than twenty modest ( $VEI < 4$ ) Holocene eruptions, knowledge of its subsurface structures, internal processes, dynamics, and their relation, is still limited.

Seismic interferometry (SI) is a high-resolution technique based on analyses of the interference of the propagated seismic energy at one or many stations. SI can be used to characterize the subsurface properties of a target area. In particular, previous SI studies performed in the area of the PPVC describe specific ranges of depth; therefore, more information is required for a thorough description of the subsurface features in the area and for a better understanding of the PPVC dynamics.

We apply SI based on autocorrelations of selected regional and teleseismic events to image the subsurface structures below stations located in

Argentina and Chile during 2012. The selection of the events is performed according to their location, magnitude, angle of incidence of P-wave seismic energy, and signal to noise ratio in the records. For each station, we extract time windows and we process them using three ranges of frequency, which are sensitive to different ranges of depths.

This work describes depths and zones previously not analyzed in the area. The results not only complement the available geological, geochemical, and geophysical information, but present new information for depths between 5 and  $\sim 400$  km depth, increasing the general knowledge of the subsurface features in the PPVC. Finally, we also propose a model for the first 45 km of the subsurface (i.e., down to the Moho), which indicates the crustal structure and the likely distribution of magma bodies in depth.

*Keywords:*

Planchón-Peteroa Volcanic Complex, Seismic Interferometry, Regional and teleseismic events, Magma storage in depth

---

## 1. Introduction

The Planchón-Peteroa Volcanic Complex -PPVC- ( $35.223^\circ$  S,  $70.568^\circ$  W; see location in [Figure 1](#)) is located in the Andes at the international border between Argentina and Chile. The PPVC is composed of three main volcanic edifices, i.e., the Azufre, the Planchón, and the Peteroa, out of which the latter is the current active volcano. The PPVC presents overlapped calderas originated from the destruction of several volcanic structures during past explosive events ([Tormey, 1989](#)). Through analyses of its historical activity and products, this volcanic system is ranked as the most hazardous volcano in Argentina ([Elissondo and Farías, 2016](#)) and the eighth most risky volcano

11 in Chile ([Technical sheet](#), Observatorio Volcanológico de los Andes del Sur,  
12 OVDAS-SERNAGEOMIN, Chile).

13 The knowledge of the PPVC has been developed by the contribution  
14 from several disciplines, i.e., geology ([Tormey, 1989](#); [Haller et al., 1994](#);  
15 [Naranjo et al., 1999](#); [Tapia Silva, 2010](#); [Haller and Risso, 2011](#)), geochemistry  
16 ([Benavente, 2010](#); [Tassi et al., 2016](#); [Benavente et al., 2016](#)), meteorology  
17 ([Guzmán et al., 2013](#)), ash analysis ([Ramires et al., 2013](#)), seismology ([Casas](#)  
18 [et al., 2014](#); [Manassero et al., 2014](#); [Olivera Craig, 2017](#); [Casas et al., 2018](#);  
19 [Casas et al.](#)), gravimetry ([Tassara et al., 2006](#)), and risk analysis ([Haller](#)  
20 [and Coscarella](#)). These studies contribute to the knowledge of the eruptive  
21 history and the current subsurface conditions of this volcanic system. Nev-  
22 ertheless, the dynamics the PPVC and their relation with the subsurface  
23 structures are still poorly understood, increasing the local risk ([Elissondo](#)  
24 [and Farías, 2016](#)).

25 A description of the subsurface structures (i.e., depth, associated dimen-  
26 sions, density contrasts, etc.) is essential for developing accurate knowl-  
27 edge of the dynamics of any volcanic system. In particular, knowledge of  
28 subsurface discontinuities provides constraints for tomographic studies, for  
29 magma-ascent modeling, among others, contributing to a better inference  
30 of the subsurface conditions, and, therefore, leading to more reliable analy-  
31 ses of likely future volcanic scenarios. Based on structural-geology analyses,  
32 [Tapia Silva \(2010\)](#) describes the subsurface geological units located in the  
33 very first 10 km of the subsurface in the area of the PPVC, and present  
34 their distribution in depth. Even though no local studies have been applied  
35 for describing the crustal structure in the PPVC, [Farías et al. \(2010\)](#) and  
36 [Giambiagi et al. \(2012\)](#) provide a crustal structure as a function of depth  
37 and the distance from the trench in the Central Andes. For the depth of

38 the subducting slab below the PPVC, they estimate four zones delimited in  
39 depth at  $\sim 12$  (the intracrustal discontinuity),  $\sim 27$ , and 45 km depth -the  
40 crust-mantle discontinuity (the Moho). The Moho is estimated at  $\sim 45$  km  
41 depth (Tassara et al., 2006); the intra-lithosphere discontinuity (top of litho-  
42 spheric low-velocity zone), at  $\sim 70$  km depth (Karato, 2012); and the top of  
43 the subducting slab, at  $\sim 120$  km depth (Tassara et al., 2006). Nevertheless,  
44 more scientific evidence is required to increase the information about the  
45 known subsurface structures, leading to a more accurate characterization of  
46 their properties, as well as to describe the subsurface features previously not  
47 analyzed. These goals motivate local studies, as the one presented in this  
48 article.

49 Claerbout (1968) has constituted a frame over which the theory of seis-  
50 mic interferometry developed. This passive seismic method -from here on,  
51 Seismic Interferometry by Autocorrelations (SIbyA)- suggests that the au-  
52 tocorrelation of a plane-wave transmission response propagating in a hori-  
53 zontally layered medium, recorded at the surface, allows the retrieval of the  
54 reflection response of a virtual source co-located to the recording station.  
55 SIbyA has shown to be a robust method; it has been applied to different  
56 type of seismic data, in several areas and at different scales. For example,  
57 SIbyA was applied to global- and teleseismic phases to imaging the crustal  
58 subsurface at regional scales (Ruigrok and Wapenaar, 2012; Nishitsuji et al.,  
59 2016), to P-wave of microseismic events to imaging the shallow volcanic sub-  
60 surface (Kim et al., 2017), and to ambient-noise seismic data at several scales  
61 (Draganov et al., 2007; Gorbatov et al., 2013; Boullenger et al., 2014; Oren  
62 and Nowack, 2017). The robustness of SIbyA has motivated its application  
63 to local (Casas et al.), regional, and teleseismic seismic data recorded in the  
64 area of the PPVC.

65 [Nishitsuji et al. \(2016\)](#) apply SIbyA to global seismic phases recorded  
66 in the eastern flank of the Peteroa volcano during 2012. They confirm the  
67 location of the Moho at  $\sim 45$  km depth, and propose a deformation feature  
68 in the subducting slab in the form of detachment, shearing, necking, or any  
69 combination of them.

70 [Casas et al.](#) apply SIbyA to local seismic events to image the subsurface  
71 below the stations located in the Argentine and Chilean sides of the PPVC  
72 during 2012. They confirm the geological structure described for the first  
73 4 km of the subsurface ([Tapia Silva, 2010](#)), provide information about re-  
74 gions of higher heterogeneity caused by faulting and complex geochemical  
75 processes, and support the presence of a magma body emplaced at  $\sim 4$  km  
76 depth (previously suggested by [Benavente \(2010\)](#)).

77 We apply SIbyA to regional and teleseismic events selected according to  
78 their location, magnitude, angles of incidence of the P-wave seismic energy  
79 at each station, and the signal to noise ratio in the records. The results  
80 for three different frequency ranges allow the description of the subsurface  
81 structures between  $\sim 5$  and 400 km depth, and the inference of the crustal  
82 structure and the location of magma bodies down to the Moho.

## 83 **2. Data**

84 The present application uses seismic data recorded by stations deployed  
85 in Argentina and Chile during 2012 (see station distribution in [Figure 1](#)).

86 The temporal deployment of seismic instruments in an area of interest is  
87 a widely used tool for reaching several goals, e.g., perform first analyses of  
88 the propagated wavefield and the subsurface conditions, increase the num-  
89 ber of the recording stations, extend the analyzed area, and improve the

90 accuracy of the results. The MalARRgue project (Ruigrok et al., 2012) was  
 91 designed by institutions from The Netherlands (Delft University of Technol-  
 92 ogy -TUDelft), Argentina (Comisión Nacional de Energía Atómica CNEA),  
 93 and The United States (Boise State University -BSU). Its goal is imaging  
 94 and monitoring the subsurface of the Malarge region (Mendoza, Argentina),  
 95 an area of high scientific interest due to peculiar volcanic and tectonic pro-  
 96 cesses (Stern, 2004). The MarlARRgue project consisted in a temporal  
 97 deployment (from January 2012 to January 2013) of 38 stations, out of  
 98 which six were deployed along the eastern flank of the PPVC (from here  
 99 on, the PV array). The PV array was equipped with short-period (2 Hz)  
 100 three-component (Sercel L-22) sensors.

101 Another source of data is provided by three broad-band stations of the  
 102 Observatorio Volcanológico de los Andes del Sur (OVDAS-SERNAGEOMIN,  
 103 Chile), which are located  $\sim 6$  km northwards. These stations (from here on,  
 104 OVDAS array) were active during 2012, through the same period as the PV  
 105 array.

### 106 3. Application and results

107 SIbyA is described by the reciprocity theorem of correlation type (Wape-  
 108 naar, 2003, 2004). Based on this theorem for transient sources (Wapenaar  
 109 and Fokkema, 2006), and using autocorrelation in the time domain, we ob-  
 110 tain:

$$\sum_{sources} \{ [T(\mathbf{x}_A, -t) * s_i(-t) * T(\mathbf{x}_A, t) * s_i(t)] \otimes [s(-t) * s(t)]_i \}$$

$$\approx -R(\mathbf{x}_A, -t) + \delta(t) - R(\mathbf{x}_A, t) \quad , \quad (1)$$

111 which states that the reflection response  $R(\mathbf{x}_A, t)$  can be retrieved at  
112 the station A located (at  $\mathbf{x}_A$ ) at the surface through the autocorrelation  
113 of a recorded transmitted wavefield  $T(\mathbf{x}_A, t)$ . The operator  $*$  indicates  
114 convolution,  $\otimes$  means deconvolution, and  $\delta$  is the Dirac's delta. The fac-  
115 tor  $[s(-t) * s(t)]_i$  corresponds to the autocorrelated source time function  
116 (ASTF), which allows the deconvolution of each source time function  $s_i(t)$ .

117 Even though [Equation 1](#) requires sources over the whole stationary phase  
118 area (i.e., the Fresnel Zone), seismic events present a non-uniform spatial  
119 distribution. Therefore, performing a selection of the seismic sources to be  
120 used is essential for a proper application of SIbyA. In order the transmission  
121 response of the propagated seismic energy to be accurately estimated by  
122 the vertical component of the records, we select only seismic events with  
123 P-wave seismic energy arriving (sub) vertically to the station at the surface.  
124 The retrieved reflection response (from here on,  $R_v(\mathbf{x}_A, t)$ ) is related to a  
125 seismic source co-located to the station at the surface, radiating P-wave  
126 energy vertically downwards.

127 A seismic source in the subsurface release energy that propagates to-  
128 wards the surface in which it is reflected. This seismic energy is reflected,  
129 refracted, and diffracted at the subsurface structures and heterogeneities (or  
130 the surface), part of which arrives to the recording station at the surface.  
131 Seismograms are then composed of direct waves followed by these reverber-  
132 ated waves. SIbyA removes the times previous to the direct arrival, and  
133 attenuates the incoherent noise, providing seismic evidence of the location  
134 of the subsurface structures. [Figure 2](#) pictures the application of SIbyA in  
135 an idealized horizontally layered 2-D medium, given a plane wavefield orig-  
136 inated by a seismic source located exactly below the station. The obtained  
137 reflection response can be used to know the depth of the reflectors located



138 in the subsurface below the station.

139 In the real Earth, nor the wave fronts are plane at local and regional  
140 scales nor the subsurface is horizontally layered in volcanic zones. In highly  
141 heterogeneous zones (as, for example, the area of the PPVC; [Manassero et al.](#)  
142 [\(2014\)](#)), the location of a seismic source exactly below the station is not an  
143 imperative condition for an accurate retrieval of the subsurface reflection  
144 response  $R_v(\mathbf{x}_A, t)$  ([Fan and Snieder, 2009](#)), i.e., the vertical component  
145 of the records is still an accurate estimation of the transmission response.  
146 Therefore, sources with small P-wave angles of incidence are selected.

### 147 *3.1. Pre-processing*

148 This section aims to get the input data and prepare it for the proper  
149 application of the [Equation 1](#). Using the reference seismic catalogs (IRIS and  
150 USGS), we select events occurred during the recording period (i.e., January  
151 2012 until January 2013) and which are characterized by a sufficiently great  
152 magnitude so that signal to noise ratio is high in the records of each station.  
153 Due to likely variations of the local seismic wavefield in space and time, we  
154 judge the signal to noise ratio of each event at each of the stations.

155 For the selection of seismic events, we use the software JWEED (Java  
156 version of Windows Extracted from Event Data) developed by IRIS. Based  
157 on restrictions in the origin time, the location, and the magnitude, we pre-  
158 select events (see [Figure 3](#)). According to their epicentral distance, we clas-  
159 sify them in two groups. One group is composed of events with epicentral  
160 distances between  $30^\circ$  and  $120^\circ$ , and magnitudes greater than Mw. 6; each  
161 event of this group guarantees a sufficiently small P-wave ray parameter  
162 ( $< 0.08$  s/km) so that seismic energy arrives (sub)vertically at the station,  
163 i.e., with incident angles  $< \sim 25^\circ$  ([Kennett et al., 1995](#)). The second group

164 is composed of events with epicentral distances lower than  $30^\circ$  and magni-  
165 tudes greater than Mw. 5. These events present a wide range of possible  
166 P-wave angles of incidence. Therefore, we perform an examination analysis  
167 on this second group in order to select only those events with at least one  
168 P-wave phase smaller than the adopted threshold (i.e.,  $0.08\text{ s/km}$ ). The ray  
169 parameters estimated by the regional velocity model ak135 (Kennett et al.,  
170 1995) are appropriate for this analysis, as smaller angles of incidence of the  
171 P-wave energy are expected in the real Earth, provided its higher hetero-  
172 geneity (Fan and Snieder, 2009). Once the seismic events are selected, there  
173 is no need to keep the distinction between the groups, i.e., they are equally  
174 significant.

175 The origin time of the selected events is used to extract the seismic  
176 waveforms from the records of the PV and OVDAS stations. A first estimate  
177 of the P- and S-wave arrival times for each event is calculated using the  
178 regional velocity model ak135. These times are then employed to manually  
179 pick accurate P- and S-wave arrival times, as well as to get the frequency  
180 range of a sufficiently high signal-to-noise ratio. We request a good ( $>$   
181 0.8) signal to noise ratio for the events to be processed, in order to avoid  
182 non-interested high amplitudes.

183 Provided the origin time of the selected events, obtained the accurate  
184 arrival times, and examined the (sub)vertical incidence of the P-wave en-  
185 ergy and high signal-to-noise ratio of the records, we extract the vertical-  
186 component records of the selected events at each of the used stations.

### 187 *3.2. Processing*

188 The vertical-component records of seismic events with P-wave energy  
189 arriving vertically at a station represent an accurate estimate of the P-wave

190 transmission response of such propagated wavefield (provided the disconti-  
191 nities are not excessively inclined; [Nishitsuji et al. \(2016\)](#)).

192 Out of the frequency range of processing previously selected for each  
193 event according to its signal to noise ratio in the results, we use those fre-  
194 quencies greater than 0.3 Hz, a threshold defined by the instrumental char-  
195 acteristics of the PV-array stations ([Nishitsuji et al., 2014](#)). Furthermore,  
196 we only use those frequencies shared through the events, i.e., [0.3 2.1] Hz.  
197 In order to perform a better interpretation of the results through depth, we  
198 segmented this frequency range in two sub-ranges, i.e., [0.3 0.8] Hz and [0.8  
199 2.1] Hz. The separating frequency (0.8 Hz) is selected after a trial and error  
200 approach, based on the observed coherency in the results for all the stations  
201 in advanced stages of the processing.

202 In order to avoid the rise of non-physical arrivals caused by cross-terms  
203 in the correlations, we extract the times between the first P-wave arrival  
204 and the first S-phase arrival. As an example, [Figure 4](#) shows the processing  
205 windows for the station PV04, for the complete range of frequencies (i.e.,  
206 [0.8 2.1] Hz).

207 The higher value of the selected frequency range (i.e., 2.1 Hz) restricts  
208 the resolution of the results for particular depths. Therefore, out of the  
209 (previously tested) vertically arriving seismic events, we make a third group  
210 composed of those with epicentral distances smaller than  $20^\circ$ . These events  
211 are characterized by a sufficiently high signal-to-noise ratio up to 3.2 Hz.  
212 As this group aims to provide information about shallower subsurface struc-  
213 tures, we select a minimum frequency of 1 Hz. Therefore, we apply the  
214 same processing workflow to the three selected frequency ranges, i.e., [0.3  
215 0.8] Hz, [0.8 2.1] Hz, and [1 3.2] Hz. As the same importance is assigned to  
216 the events of each of the three groups, we normalize the processing windows

217 according to their vertical flux of seismic energy.

218 As suggested by [Equation 1](#), we estimate and deconvolve the ASTF  
219 from each of the autocorrelated time windows. The ASTF of each event is  
220 estimated by the main lobe and the secondary monotonous-decreasing lobes,  
221 as shown in [Figure 5](#) for the station AD2 and the frequency range [0.3 0.8]  
222 Hz.

223 [Figure 6](#) presents the autocorrelation of the time windows for the station  
224 PV01 and the frequency range [0.3 0.8] Hz, in which each trace is decon-  
225 volved by its previously estimated ASTF. This figure shows the dominance  
226 of the main lobe in the autocorrelated deconvolved traces. These features  
227 close to 0 s are mainly non-physical amplitudes remaining from the decon-  
228 volution. Therefore, these amplitudes are removed through windowing.

229 SIbyA is based on the autocorrelation of time windows extracted from  
230 the records of selected seismic events. Note that the autocorrelation of  
231 a extracted time window could arise non-physical arrivals at times equal  
232 to the time interval between two P-wave arrivals, reducing the quality of  
233 the results. However, these time intervals are a function of the epicentral  
234 distance of the events. The seismic events used in this application present  
235 a wide range of epicentral distances, so that the non-physical arrivals are  
236 located at different times in the autocorrelations, leading to a destructive  
237 interference of their energy during stacking (see [Figure 7](#)).

238 The last step in the application of [Equation 1](#) is stacking the resulting  
239 seismic traces for each station, which enhances the energy from the sta-  
240 tionary phase area. [Figure 8](#) shows the pre-stack panel (deconvolved and  
241 windowed traces) and the stacked traces for stations AD2 and PV04, for the  
242 three selected frequency ranges of processing.

#### 243 4. Interpretation and discussion

244 Aiming to compare the seismic results with the known features of the  
245 subsurface, we transform the time vector of the results to depth through  
246 construction and utilization of a velocity model. This model is composed of  
247 velocities provided by the regional model ak135 for depths greater than 60  
248 km, and a modified version of the one obtained by [Bohm et al. \(2002\)](#) for  
249 shallower depths (see used velocity model in [Figure 9](#)).

250 [Figure 10](#) and [Figure 11](#) show the stacked traces for the PV and OV-  
251 DAS arrays, respectively, for each processing frequency range. These figures  
252 also show the interpreted subsurface features for each of the stations. As a  
253 complex impedance contrast through depth is expected for the area of the  
254 PPVC, we only seek for the dominant amplitudes on the obtained reflection  
255 responses, which are potentially related to the main subsurface discontinu-  
256 ities. The lower frequency range (i.e., [0.3 0.8] Hz) leads to describe the  
257 subsurface between  $\sim 40$  and 400 km depth. The results for the other two  
258 frequency ranges (i.e., [0.8 2.1] Hz, and [1 3.2] Hz) allow to interpret the  
259 subsurface features for depths between 5 and  $\sim 45$  km. The minimum depth  
260 limit is set by the non-physical amplitudes removed from close to 0 s after  
261 deconvolution. The maximum depth limit is set by the coherency in the  
262 results for all the frequency ranges and all the used stations.

263 The interpretation of the results for the smallest frequency range ([0.3  
264 0.8] Hz) is performed through contrast of the seismic results and the expected  
265 location of the known subsurface features based on the geodynamic scenario  
266 and the available geological information for the area of the PPVC ([Ferrán  
267 and Martínez, 1962](#); [Tassara et al., 2006](#); [Benavente, 2010](#); [Tapia Silva, 2010](#);  
268 [Karato, 2012](#)).

269 The results for the PV array (see [Figure 10a](#)) show six dominant ampli-  
270 tudes (i.e., local maximum on the absolute values of the waveforms), which  
271 we classify as potential subsurface discontinuities. The close location of the  
272 identified features in the seismic results and the known subsurface features  
273 lead to the interpretation of the Mohorovicic discontinuity at  $\sim 45$  km depth,  
274 the intra-lithospheric discontinuity at 65 km, the top of the subducting slab  
275 between 110 and 120 km, the bottom of the subducting slab between 140  
276 and  $\sim 160$  km, the lithosphere-asthenosphere boundary between 230 and 255  
277 km, and the top of the asthenospheric low-velocity zone between  $\sim 330$  and  
278  $\sim 360$  km depth.

279 The OVDAS array (see [Figure 11a](#)) is an array located  $\sim 6$  km to the  
280 north of the PV array, composed of half the stations of the latter, and  
281 with greater longitudinal extension. The results for the OVDAS array al-  
282 low to interpret the Mohorovicic discontinuity at  $\sim 45$  km depth, the intra-  
283 lithospheric discontinuity between 70 and 90 km, the top of the subducting  
284 slab between 115 and 130 km, the bottom of the subducting slab between  
285  $\sim 165$  and  $\sim 185$  km, the lithosphere-asthenosphere boundary at  $\sim 250$  km,  
286 and the top of the asthenospheric low-velocity zone between  $\sim 310$  and  $\sim 350$   
287 km depth.

288 Based on the seismic velocity values for the depths of interpretation and  
289 the frequency range of processing, the resolution of the seismic results is 5  
290 km ([Widess, 1973](#)). This value leads to interpret that the results for the  
291 OVDAS array do not differ substantially from the results of the PV array,  
292 what is expected provided the small geological variation in  $\sim 6$  km along  
293 the north-south direction for the used processing wavelengths. The best  
294 correlation in depth is observed for the Mohorovicic discontinuity (43-48 km  
295 depth), the lithosphere-asthenosphere boundary ( $\sim 245$  km), and the top

296 of the asthenospheric low-velocity zone ( $\sim 340$  km). A small difference in  
297 depth is observed for the intra-lithospheric discontinuity and the top of the  
298 subducting slab; even though greater depths are observed in the results of  
299 the OVDAS stations, these differences would not be significant based on  
300 the vertical resolution of the results. A greater difference is observed for the  
301 bottom of the subducting slab, i.e.,  $\sim 15$  km greater for the OVDAS stations.

302 Although a dominant positive arrival is expected at the depth of the  
303 Moho, a dominant negative amplitude is retrieved in the results for most  
304 of the stations. Based on the retrieved waveforms, we interpret the pres-  
305 ence of a complex area at  $\sim 40$ - $55$  km depth, causing a perturbation of the  
306 amplitudes retrieved for these depths, in particular for those related to the  
307 Moho.

308 Even though dipping structures in the subsurface restrict the reflection  
309 energy arrived at the surface, we clearly recognize the depth of the top and  
310 bottom of the subducting slab. Therefore, two hypotheses arise. One hy-  
311 pothesis suggests a stair-like subduction, according to which the top and the  
312 bottom of the oceanic slab present horizontal (or gently inclined) regions;  
313 the different depths estimated in the results of the PV and the OVDAS ar-  
314 rays for the bottom of the subducting slab could be caused by a local change  
315 of the thickness of the subducting lithosphere. Nevertheless, this hypothesis  
316 would not explain the lack of seismicity at the longitude of the stations and  
317 depths of analysis (*US Geological Survey*; Nishitsuji et al. (2016)). A second  
318 hypothesis (Nishitsuji et al., 2016) proposes a slab deformation in the form  
319 of detachment, shearing, necking, or any combination. Then, a differential  
320 deformation between the latitudes of the PV and OVDAS arrays would ex-  
321 plain the estimated depths for the bottom of the subducting slab. Finally,  
322 more information is required to elucidate the proper interpretation.

323 For the two higher ranges of frequencies (i.e., [0.8 2.1] Hz and [1 3.2] Hz)  
324 (see [Figure 10b](#), [Figure 10c](#), [Figure 11b](#), and [Figure 11c](#)), the interpretation  
325 is also based on the identification of the dominant amplitudes in the results,  
326 and the depths for which the arrived reflected energy is particularly smaller,  
327 a feature probably caused by the emplacement of a sufficiently great volume  
328 of magma as to be manifested in the seismic results.

329 The results for the PV array and the frequency range [0.8 2.1] Hz (see  
330 [Figure 10b](#)) indicate five clear dominant arrivals in most of the stations, out  
331 of which four are between  $\sim 10$  and  $\sim 30$  km depth and another one at  $\sim 40$  km  
332 depth. Additionally, we identify an apparent lack of dominant amplitudes  
333 for depths between  $\sim 30$  and  $\sim 40$  km (indicated with an arrow in [Figure 10b](#)).  
334 The features identified for [0.8 2.1] Hz are supported by the results for the  
335 frequency range [1 3.2] Hz ([Figure 10c](#)), which improve the depth of the  
336 inferred subsurface discontinuities. In addition, these results manifest an  
337 apparent low-amplitude region at  $\sim 25$  km depth for the western stations of  
338 the array. The results for this frequency range also show a dominant arrival  
339 at  $\sim 6$  km depth.

340 The results for the OVDAS stations agree with the interpretation per-  
341 formed for the PV array, for the two analyzed frequency ranges. Therefore,  
342 we identify local-maximum amplitudes, as well as apparent small-amplitude  
343 zones, at roughly the same depths for the two arrays and for the two higher-  
344 frequency ranges, even though the effect of attenuation increases for the  
345 highest frequencies (around 3 Hz in this application) ([Schön, 2015](#)). Then,  
346 these results allow the interpretation of the subsurface structures between 5  
347 and  $\sim 45$  km depth (the Moho).

348 Based on the average depth of the reflectors interpreted in the seismic re-  
349 sults, the available scientific information about the subsurface in the PPVC,



350 the proposed structure of the crust for the Central Andes (Farías et al.,  
351 2010; Giambiagi et al., 2012), and the physics of magma storage in the crust  
352 Jackson et al. (2018), we propose a model for the distribution of magma  
353 reservoirs in depth in relation to the main subsurface structures in the crust  
354 (see Figure 12).

355 Through comparison of the average depth of the interpreted reflectors  
356 below the stations and the proposed structure of the crust (Farías et al.,  
357 2010; Giambiagi et al., 2012), we associate the interpreted reflectors at  $\sim 12$ ,  
358  $\sim 18$ , and  $\sim 32$  km depth as the intra-crustal discontinuity (rigid-ductile dis-  
359 continuity in the upper crust), the discontinuity between the upper and lower  
360 crust, and the rigid-ductile discontinuity in the lower crust, respectively (see  
361 Figure 12).

362 Jackson et al. (2018) models the formation, storage, and chemical differ-  
363 entiation of magma in the Earth’s crust. According to the physics of magma  
364 storage, the melt fraction is not homogeneously distributed through depth.  
365 A great percentage of melt is located in the very upper part of a reservoir,  
366 a low percentage is located through most of the reservoir, while a solid area  
367 is present in the lower part. The seismic results are most probably evidence  
368 of the solid lower section of the reservoir (Jackson et al., 2018). Therefore,  
369 we interpret a region in depth as characterized by a magma emplacement  
370 in case two conditions are satisfied: 1. the presence of an area of smaller  
371 amplitudes in the seismic results, and 2. it is located above any of the inter-  
372 preted subsurface reflectors. This circumstance is satisfied for two regions,  
373 i.e., a shallower zone located above the rigid-ductile discontinuity in the  
374 lower crust (i.e.,  $\sim 32$  km depth); and a deeper one at  $\sim 35$  km depth, above  
375 a reflector located at  $\sim 40$  km.

376 Even though no amplitude information is available for depths lower than

377 5 km depth (which are removed after deconvolution), a subsurface model for  
378 the area (Benavente, 2010) proposes a magma emplacement at  $\sim 4$  km depth.  
379 We identify a reflector at  $\sim 6$  km depth, which motivates the incorporation  
380 of such magma emplacement in our model.

381 Furthermore, two regions (indicated with a question mark in Figure 12)  
382 satisfy only one of the imposed conditions, therefore, their interpretation as  
383 regions of magma storage is subjected to extra information. These regions  
384 are located above the reflectors interpreted at  $\sim 22$  km depth and the Moho,  
385 for which no apparent smaller amplitudes are observed, probably due to  
386 its close location to another feature of the subsurface (upper-lower crust  
387 discontinuity and the Moho, respectively), or the resolution of the seismic  
388 results are not sufficiently great to recognize a region of limited vertical  
389 extension of magma.

390 Our results support the information obtained for the subsurface in the  
391 area (Yuan et al., 2006; Ward et al., 2013; González-Vidal et al., 2018)  
392 which indicate (although with a limited resolution) low-velocity zones for  
393 approximately the same range of depths. They are also consistent with  
394 the conceptual model proposed for the area (Benavente, 2010) for depths  
395 between 5 and 15 km depth, for which great volumes of magma storage are  
396 not expected.

397 Finally, more research (e.g., local seismic velocity -or attenuation- tomog-  
398 raphy studies) is required to accurately identify the location and dimensions  
399 of the regions of magma emplacement.

400 **5. Conclusions**

401 Even though the Planchón-Peteroa Volcanic Complex (PPVC) is one of  
402 the most hazardous volcanic systems in the Central Andes, knowledge of  
403 its internal processes, structures, dynamics, and their relation are still not  
404 satisfactorily understood.

405 We apply seismic interferometry by autocorrelations to regional and tele-  
406 seismic data recorded by nine stations deployed in the area of the PPVC (six  
407 in Argentina and three in Chile) during 2012. The events are selected accord-  
408 ing their location, magnitude, angle of incidence of the P-wave energy, the  
409 signal to noise ratio on the results, and the related useful frequency range.  
410 In order to perform an appropriate description of the subsurface structures  
411 below the stations, we use three frequency ranges ([0.3 0.8] Hz, [0.8 2.1] Hz,  
412 and [1 3.2] Hz) which are sensitive to different range of frequencies.

413 The smallest frequency range ([0.3 0.8] Hz) is used to infer the tectonic  
414 features, i.e., the Moho (at 43-48 km depth), the intra-lithospheric discon-  
415 tinuity ( $\sim 70$  km), the top and bottom of the subducting slab ( $\sim 120$  and  
416  $\sim 150$ -165 km), the lithosphere-asthenosphere boundary ( $\sim 250$  km), and the  
417 top of the asthenospheric low-velocity zone ( $\sim 340$  km). The results support  
418 the hypothesis of deformation in the form of detachment, searing, and/or  
419 necking for the longitude of the used stations. Our results also suggest a  
420 higher depth ( $\sim 15$  km) for the bottom of the subducting slab at the north  
421 of the PPVC, likely caused by differential deformation along the latitude  
422 direction.

423 Based on the results for the two higher-frequency ranges ([0.8 2.1] Hz  
424 and [1 3.2] Hz) and previous geological, geochemical, and geophysical infor-  
425 mation, we propose a model which describes the structure of the crust and

426 the subsurface regions storing magma bodies down to the Moho. Three  
427 regions of sufficiently great volume of magma emplaced at  $\sim 4$  km,  $\sim 28$  km,  
428 and  $\sim 35$  km depth, respectively are indicated.

429 The present work provides valuable information about the subsurface  
430 conditions of an active volcanic system -the CVPP. We expect the obtained  
431 knowledge to be employed in future research aiming to better understand  
432 the dynamics of the CVPP.

### 433 **References**

434 Benavente, O., 2010. Actividad Hidrotermal asociada a los Complejos  
435 Volcánicos Planchón-Peteroa y Descabezado Grande-Quizapu-Cerro Azul,  
436 36S y 37°S, Zona Volcánica Sur, Chile. Universidad de Chile .

437 Benavente, O., Tassi, F., Reich, M., Aguilera, F., Capecchiacci, F.,  
438 Gutiérrez, F., Vaselli, O., Rizzo, A., 2016. Chemical and isotopic fea-  
439 tures of cold and thermal fluids discharged in the Southern Volcanic Zone  
440 between 32.5S and 36S: Insights into the physical and chemical processes  
441 controlling fluid geochemistry in geothermal systems of Central Chile.  
442 Chemical Geology .

443 Bohm, M., Lüth, S., Echtler, H., Asch, G., Bataille, K., Bruhn, C., Riet-  
444 brock, A., Wigger, P., 2002. The Southern Andes between 36 and 40S  
445 latitude: Seismicity and average seismic velocities. Tectonophysics .

446 Boullenger, B., Verdel, A., Paap, B., Thorbecke, J., Draganov, D., 2014.  
447 Studying CO<sub>2</sub> storage with ambient-noise seismic interferometry: A com-  
448 bined numerical feasibility study and field-data example for Ketzin, Ger-  
449 many. Geophysics 80, Q1–Q13.

- 450 Casas, J.A., Badi, G., Manassero, M., Gomez, P., Draganov, D., Ruzzante,  
451 J., 2014. Characterization of Seismo-volcanic Activity in Peteroa Volcano,  
452 Central Andes Argentina-Chile. *Earth Sciences Research Journal* 18, 335–  
453 336.
- 454 Casas, J.A., Draganov, D., Badi, G., Manassero, M.C., Olivera Craig, V.,  
455 Franco, L., Gómez, M., Ruigrok, E., . Seismic interferometry applied to  
456 local fracture seismicity recorded at Planchón-Peteroa Volcanic Complex,  
457 Argentina-Chile. Manuscript under revision .
- 458 Casas, J.A., Mikesell, T.D., Draganov, D., Lepore, S., Badi, G.A., Franco,  
459 L., Gómez, M., 2018. Shallow S-Wave Velocity Structure from Ambient  
460 Seismic Noise at Planchón-Peteroa Volcanic Complex, Argentina-Chile.  
461 *Bulletin of the Seismological Society of America* 108, 2183–2198.
- 462 Claerbout, J.F., 1968. Synthesis of a layered medium from its acoustic  
463 transmission response. *GEOPHYSICS* .
- 464 Draganov, D.S., Wapenaar, K., Mulder, W., Singer, J., Verdel, A., 2007. Re-  
465 trieval of reflections from seismic background-noise measurements. *Geo-*  
466 *physical Research Letters* 34.
- 467 Elissondo, M., Farías, C., 2016. Volcanic Risk assessment in Argentina, in:  
468 *Cities on Volcanoes IX*, Puerto Varas, Chile.
- 469 Fan, Y., Snieder, R., 2009. Required source distribution for interferometry  
470 of waves and diffusive fields. *Geophysical Journal International* 179, 1232–  
471 1244.
- 472 Farías, M., Comte, D., Charrier, R., Martinod, J., David, C., Tassara, A.,  
473 Tapia, F., Fock, A., 2010. Crustalscale structural architecture in central

- 474 Chile based on seismicity and surface geology: Implications for Andean  
475 mountain building. *Tectonics* 29.
- 476 Ferrán, O.L.G., Martínez, M.V., 1962. Reconocimiento geológico de la  
477 Cordillera de los Andes entre los paralelos 35 y 38 sur, in: *Anales de*  
478 *la Facultad de Ciencias Físicas y Matemáticas*, pp. 1–19.
- 479 Giambiagi, L., Mescua, J., Bechis, F., Tassara, A., Hoke, G., 2012. Thrust  
480 belts of the southern Central Andes: Along-strike variations in shortening,  
481 topography, crustal geometry, and denudation. *Bulletin of the Geological*  
482 *Society of America* .
- 483 González-Vidal, D., Obermann, A., Tassara, A., Bataille, K., Lupi, M.,  
484 2018. Crustal model of the Southern Central Andes derived from ambient  
485 seismic noise Rayleigh-wave tomography. *Tectonophysics* .
- 486 Gorbatov, A., Saygin, E., Kennett, B.L., 2013. Crustal properties from  
487 seismic station autocorrelograms. *Geophysical Journal International* .
- 488 Guzmán, C., Huacailuk, C., Tamasi, M., Martínez Bogado, M., Torres,  
489 D., 2013. Anomalías Encontradas en los Parámetros Registrados en la  
490 Estación de Medición de la Terma del Volcán Peteroa, in: *Actas de ICES*  
491 *IX*, pp. 186–194.
- 492 Haller, M.J., Coscarella, M., . Análisis probabilístico del riesgo de erupción  
493 del volcán Peteroa mediante la aplicación de mezcla de distribuciones  
494 exponenciales. *Nat. Hazards Earth Syst. Sci* 9, 425–431.
- 495 Haller, M.J., Ostera, H.A., Pesce, A.H., Gardini, M., Folguera, A., 1994.  
496 Vulcanoestratigrafía reciente y eruptividad del volcán Peteroa, in: *Con-*  
497 *greso Geológico Chileno*, pp. 319–323.

498 Haller, M.J., Risso, C., 2011. La erupción del volcán peteroa (3515's, 7018'o)  
499 del 4 de septiembre de 2010. Revista de la Asociacion Geologica Argentina  
500 .

501 Jackson, M.D., Blundy, J., Sparks, R.S., 2018. Chemical differentiation,  
502 cold storage and remobilization of magma in the Earth's crust.

503 Karato, S.I., 2012. On the origin of the asthenosphere. Earth and Planetary  
504 Science Letters [arXiv:1104.0048v2](https://arxiv.org/abs/1104.0048v2).

505 Kennett, B.L.N., Engdahl, E.R., Buland, R., 1995. Constraints on seismic  
506 velocities in the Earth from traveltimes. Geophysical Journal International  
507 .

508 Kim, D., Brown, L.D., Árnason, K., Ágústsson, K., Blanck, H., 2017.  
509 Magma reflection imaging in Krafla, Iceland, using microearthquake  
510 sources. Journal of Geophysical Research: Solid Earth .

511 Manassero, M., Badi, G., Casas, J.A., Gomez, M., Draganov, D., Ruzzante,  
512 J., 2014. Seismic attenuation around Peteroa Volcano, Argentina. Earth  
513 Sciences Research Journal 18, 341–342.

514 Naranjo, J.A., Haller, M.J., Ostera, H.A., Pesce, A.H., Sruoga, P., 1999.  
515 Geologia y peligros del Complejo Volcánico Planchón-Peteroa, Andes del  
516 Sur (3515'S), Región del Maule, Chile-Provincia de Mendoza, Argentina.  
517 Servicio Nacional de Geología y Minería.

518 Nishitsuji, Y., Ruigrok, E., Gomez, M., Draganov, D., 2014. Global-phase  
519 H/V spectral ratio for delineating the basin in the Malargue Region, Ar-  
520 gentina. Seismological Research Letters 85, 1004–1011.

- 521 Nishitsuji, Y., Ruigrok, E., Gomez, M., Wapenaar, K., Draganov, D., 2016.  
522 Reflection imaging of aseismic zones of the Nazca slab by global-phase  
523 seismic interferometry. Interpretation 4, SJ1–SJ16.
- 524 Olivera Craig, V., 2017. Relocation of fracture seismicity in Planchón-  
525 Peteroa Volcanic Complex through optimization of the arrival-times iden-  
526 tification and joint location techniques. Ph.D. thesis.
- 527 Oren, C., Nowack, R.L., 2017. Seismic body-wave interferometry using noise  
528 autocorrelations for crustal structure. Geophysical Journal International  
529 .
- 530 Ramires, A., Elissonde, A., Trombotto Liaudat, D., 2013. Posibles escenarios  
531 de riesgo frente a la caída de cenizas volcánicas, en el modelo ganadero  
532 de la cuenca alta y media del Rio Grande, Malargüe, Mendoza, in: Actas  
533 de IX, pp. 304–320.
- 534 Ruigrok, E., Draganov, D., Gomez, M., Ruzzante, J., Torres, D., Pumarega,  
535 I.L., Barbero, N., Ramires, A., Ganan, A.R.C., van Wijk, K., 2012.  
536 Malargüe seismic array: Design and deployment of the temporary array.  
537 The European Physical Journal Plus 127, 126.
- 538 Ruigrok, E., Wapenaar, K., 2012. Global-phase seismic interferometry un-  
539 veils P-wave reflectivity below the Himalayas and Tibet. Geophysical  
540 Research Letters 39.
- 541 Schön, J.H., 2015. Physical properties of rocks: Fundamentals and principles  
542 of petrophysics. volume 65. Elsevier.
- 543 Stern, C.R., 2004. Active Andean volcanism: its geologic and tectonic set-  
544 ting. Revista geológica de Chile .



- 545 Tapia Silva, F.F., 2010. Análisis estructural del sector occidental de la faja  
546 plegada y corrida de Malargüe en el curso superior del río Colorado de  
547 Lontué (35 18'y 35°23's), Región del Maule, Chile. Universidad de Chile  
548 .
- 549 Tassara, A., Götze, H.J., Schmidt, S., Hackney, R., 2006. Three-dimensional  
550 density model of the Nazca plate and the Andean continental margin.  
551 Journal of Geophysical Research: Solid Earth .
- 552 Tassi, F., Aguilera, F., Benavente, O., Paonita, A., Chiodini, G., Caliro,  
553 S., Agosto, M., Gutierrez, F., Capaccioni, B., Vaselli, O., Caselli, A.,  
554 Saltori, O., 2016. Geochemistry of fluid discharges from Peteroa volcano  
555 (Argentina-Chile) in 2010-2015: Insights into compositional changes re-  
556 lated to the fluid source region(s). Chemical Geology .
- 557 Tormey, D., 1989. Geologic history of the active Azufre-Planchon-Peteroa  
558 volcanic center (3515'S, Southern Andes) with implications for the devel-  
559 opment of compositional gaps. Asoc. Gel. Arg. Rev , 420–430.
- 560 Wapenaar, K., 2003. Synthesis of an inhomogeneous medium from its acous-  
561 tic transmission response. GEOPHYSICS .
- 562 Wapenaar, K., 2004. Retrieving the elastodynamic Green's function of an  
563 arbitrary inhomogeneous medium by cross correlation. Physical Review  
564 Letters 93.
- 565 Wapenaar, K., Fokkema, J., 2006. Green's function representations for seis-  
566 mic interferometry. GEOPHYSICS .
- 567 Ward, K.M., Porter, R.C., Zandt, G., Beck, S.L., Wagner, L.S., Minaya, E.,

568 Tavera, H., 2013. Ambient noise tomography across the Central Andes.  
569 Geophysical Journal International .

570 Widess, M.B., 1973. How thin is a thin bed? GEOPHYSICS .

571 Yuan, X., Asch, G., Bataille, K., Bock, G., Bohm, M., Echtler, H., Kind,  
572 R., Oncken, O., Wölbern, I., 2006. Deep seismic images of the Southern  
573 Andes. Geological Society of America Special Papers .

574 **6. Figures**

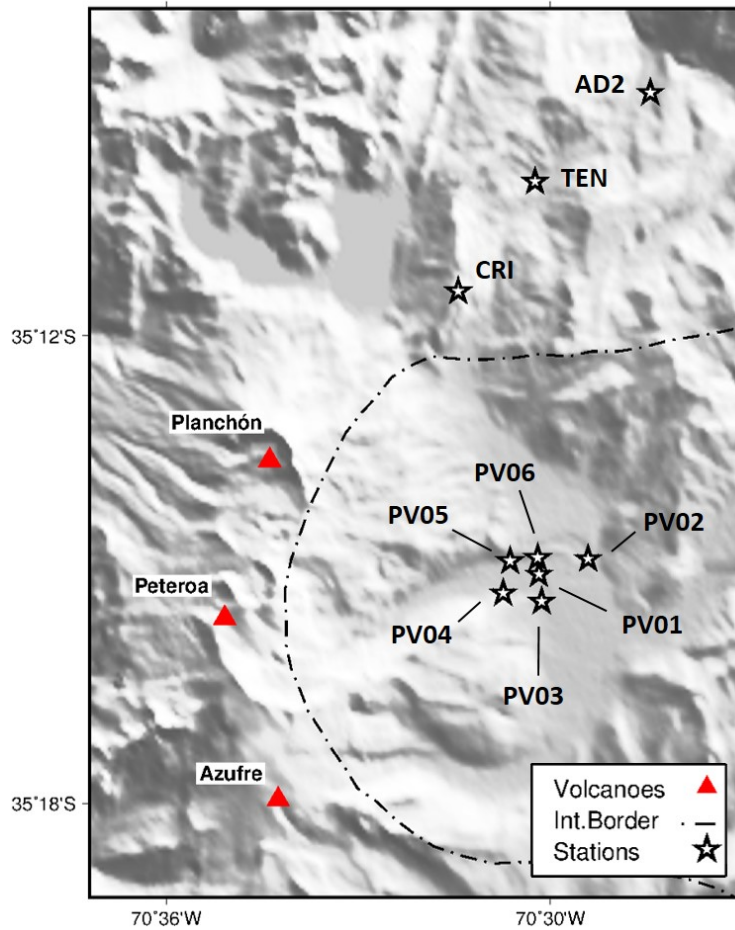


Figure 1: Distribution of the seismic stations used in the present application in relation to the main edifices of the Planchón-Peteroa Volcanic Complex (PPVC).

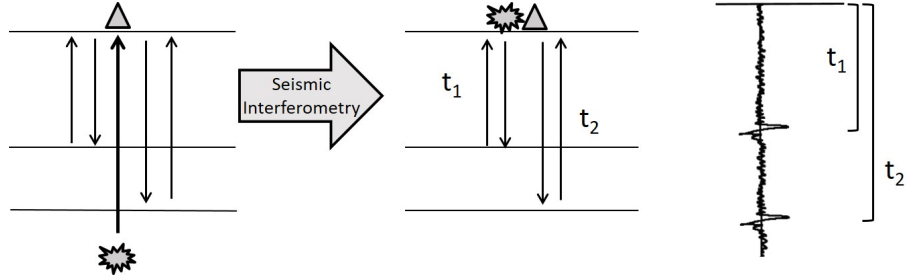


Figure 2: Seismic interferometry by autocorrelation applied to vertically arriving energy in a horizontally layered medium.  $t_j$  represents the two-way travel time between the station at the surface and the reflector  $j$  in the subsurface. The autocorrelation allows the retrieval of a seismogram composed of reflected energy released by a virtual source co-located at the position of the station.

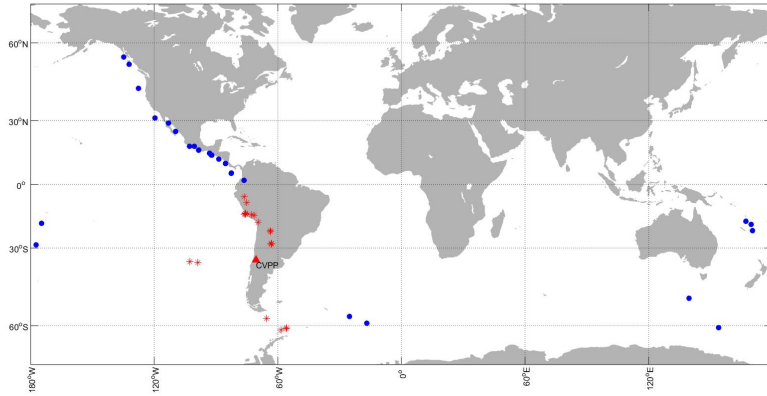


Figure 3: Location of seismic events pre-selected for the application of SIbyA in the area of the PPVC. A triangle indicates the location of the PPVC. Stars show the location of events with epicentral distances less than  $30^\circ$  and magnitudes  $M_w > 5$ . Circles indicate events with epicentral distances greater than  $30^\circ$  and less than  $120^\circ$ , and magnitudes  $M_w > 6$ .

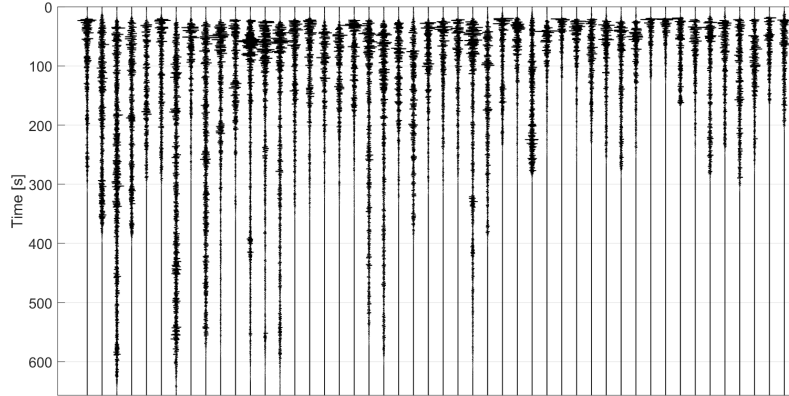


Figure 4: Processing time windows (P-wave codas) for each of the events selected for PV04 station in the complete range of frequencies, i.e.,  $[0.3 \text{ } 2.1]$  Hz. Each window is normalized according to its vertical energy flux. Vertical axis indicates propagation time. Each window is composed of a pre-event time (20 s) and the times between the first P- and S-wave arrival times.

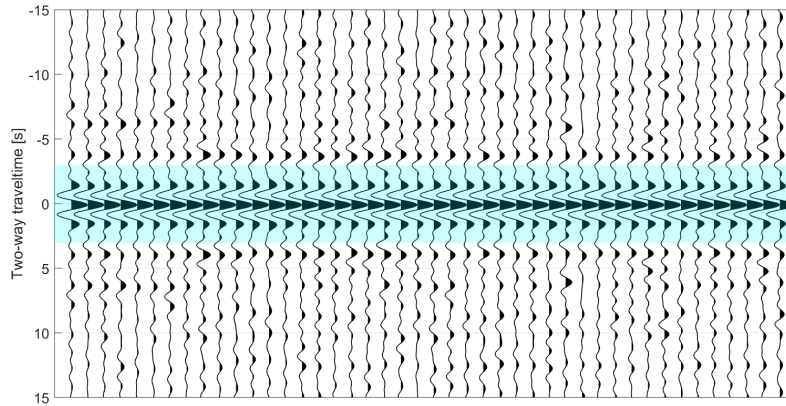


Figure 5: Autocorrelated source time functions (ASTFs) estimated for the station AD2 for the frequency range  $[0.3 \text{ } 0.8]$  Hz. A shaded area shows the ASTFs in the autocorrelation panel (for graphical purposes, we only show the first 15 s).

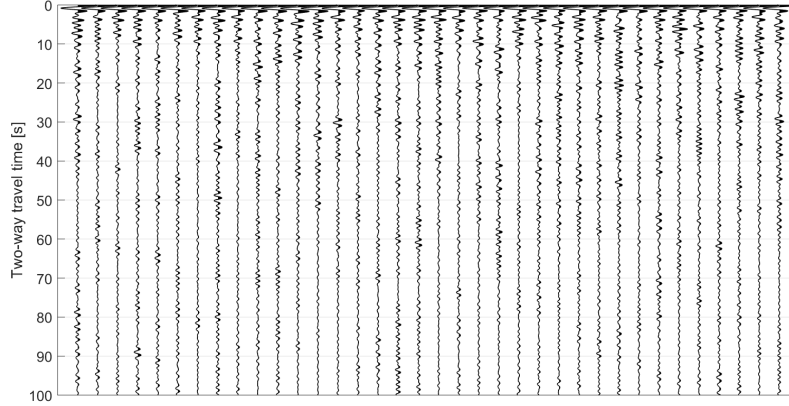


Figure 6: Autocorrelated time windows for the station PV01 in the frequency range [0.3 0.8] Hz. The vertical axis indicates two-way travel time. Each seismic trace is deconvolved by its previously estimated source time function.

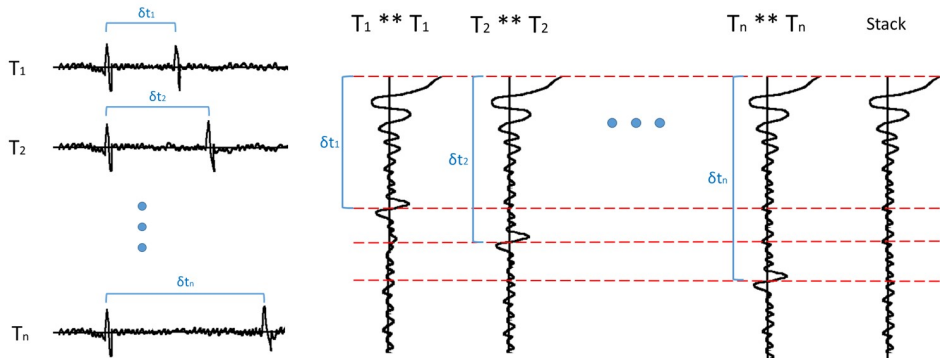
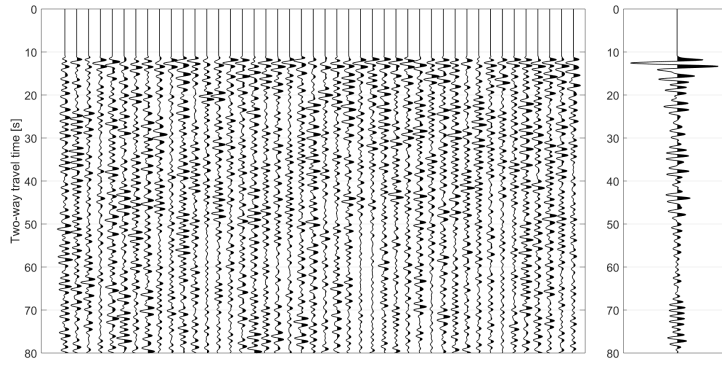
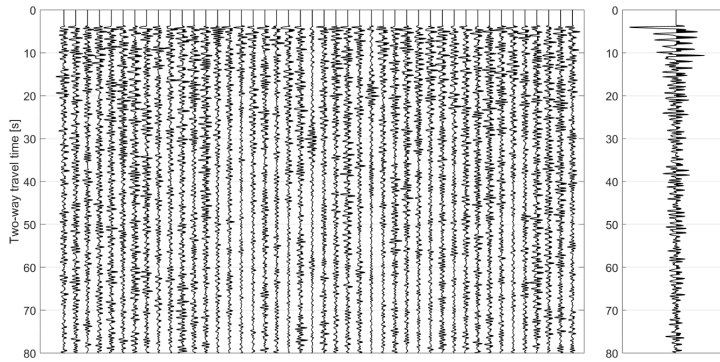


Figure 7: Cartoon illustrating the attenuation of non-physical arrivals originated in the correlation of a time window with several P-wave arrivals. Stacking seismic traces from events with different epicentral distances enhances features located in phase, so that non-physical arrivals due to several P-wave arrivals are attenuated. Without loss of generality, this figure shows the effect of stacking using time windows of events with different epicentral distances, each of them composed of two P-wave phases.  $T_i$  is the time window of the event  $i$ , which contains two P-wave arrivals separated in  $\delta t_i$ . Operator  $**$  means correlation. Dashed lines indicate equal time values.

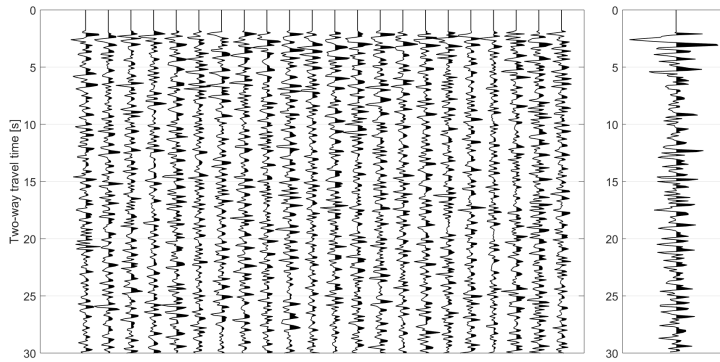
(a) AD2 [0.3 0.8] Hz



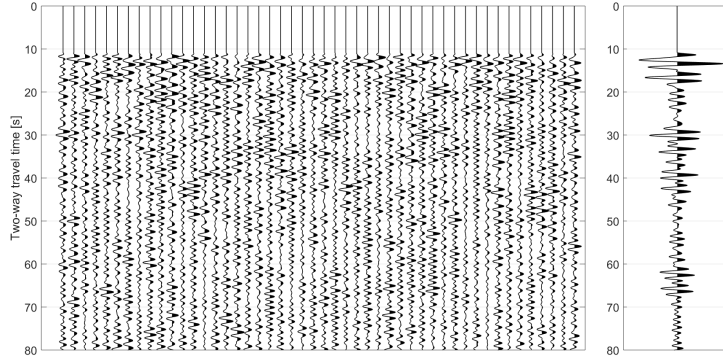
(b) AD2 [0.8 2.1] Hz



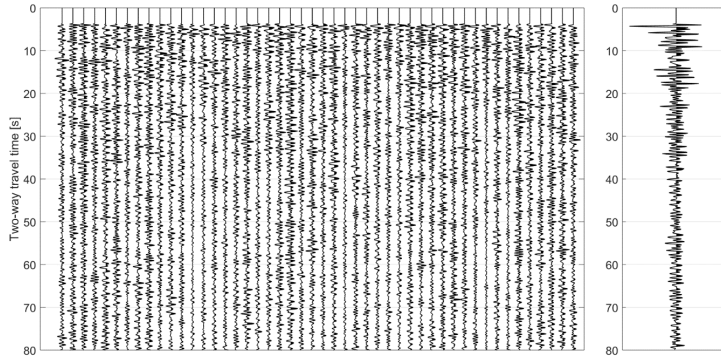
(c) AD2 [1 3.2] Hz



(d) PV04 [0.3 0.8] Hz



(e) PV04 [0.8 2.1] Hz



(f) PV04 [1 3.2] Hz

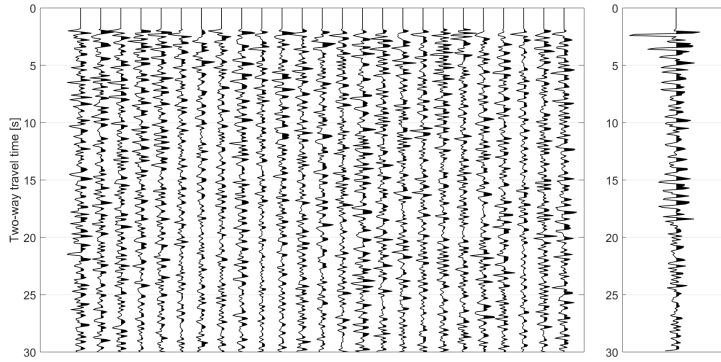


Figure 8: Pre-stacking panels and stacked seismic trace for the stations AD2 (a, b, c) and PV04 (d, e, f), for the frequency ranges [0.3 0.8] Hz (a, d), [0.8 2.1] Hz (b, e), and [1 3.2] Hz (c, f).



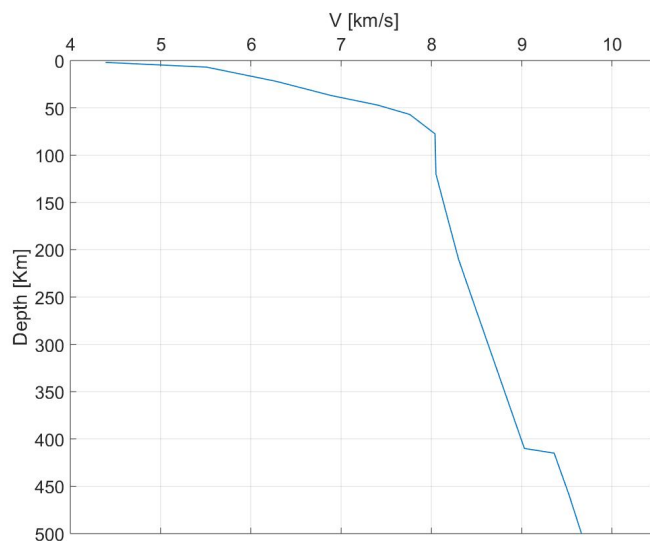


Figure 9: Velocity model used to perform the time-to-depth transformation of the seismic results.

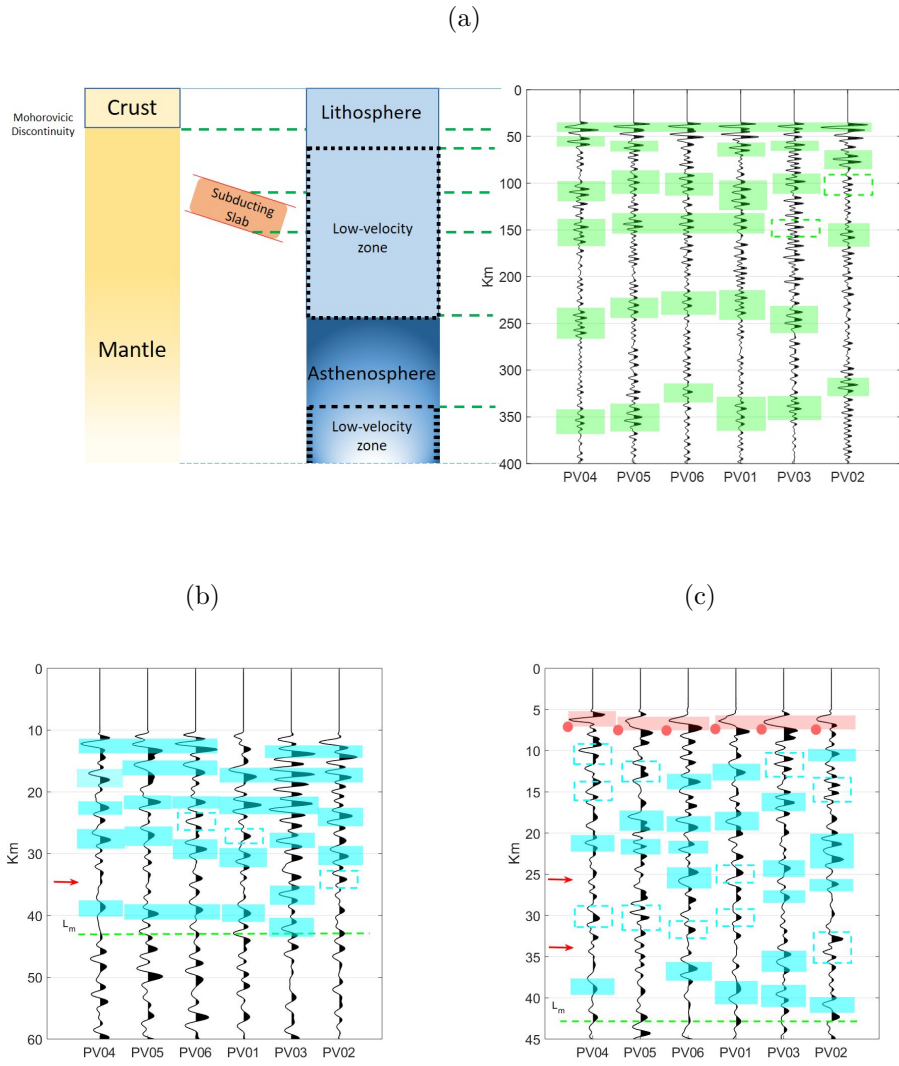


Figure 10: Interpretation of the results at the stations of the PV array for the three frequency ranges: (a) [0.3 0.8] Hz, (b) [0.8 2.1] Hz, y (c) [1 3.2] Hz. Filled rectangle areas show the local maximum amplitudes, i.e., the interpreted subsurface discontinuities below each station. Rectangles with dashed line borders indicate a higher uncertainty at the identification of a discontinuity. Discontinuities interpreted only in (c) are marked with a small circle in the left bottom corner of each rectangle. Figure 10c also shows the interpreted discontinuities at depths close to those interpreted in (b).  $L_m$  represent the minimum depth level for the Moho (interpreted in (a)). Arrows indicate zones of likely emplacement of magma.



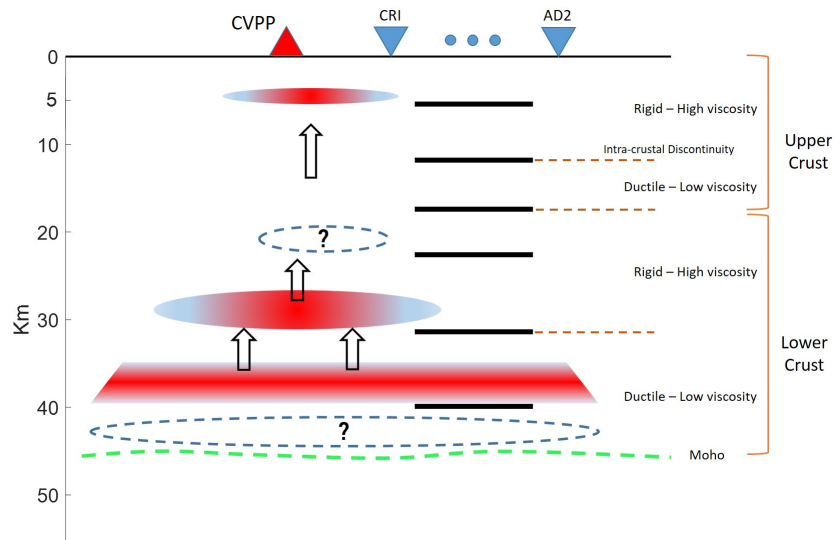


Figure 12: Proposed model of magma emplacement in relation to the structure of the crust down to the Moho in the area of the PPVC. Inverted triangles indicate the longitude of the stations. Thick horizontal lines below the stations show the average depth of the reflectors interpreted in the seismic results. Dashed lines are the interpreted discontinuities (based on [Farías et al. \(2010\)](#) and [Giambiagi et al. \(2012\)](#)) between the different regions of the crust. Arrows show the inferred direction of magma movement. Areas with a question mark inside indicate zones of higher ambiguity in the interpretation.